Postprint of: Białobrzeska W., Głowacki M.J., Janik M., Ficek M., Pyrchla K., Sawczak M., Bogdanowicz R., Malinowska N., Żołędowska S., Nidzworski D., Quantitative fluorescent determination of DNA – Ochratoxin a interactions supported by nitrogen-vacancy rich nanodiamonds, Journal of Molecular Liquids, Vol. 342 (2021), 117338, DOI: 10.1016/j.molliq.2021.117338

Quantitative fluorescent determination of DNA – Ochratoxin A interactions supported by nitrogen-vacancy rich nanodiamonds

Wioleta Białobrzeska[1], Maciej J. Głowacki[2], Monika Janik[2,3], Mateusz Ficek[2], Krzysztof Pyrchla[2], Mirosław Sawczak[4], Robert Bogdanowicz[2], Natalia Malinowska[1], Sabina Żołędowska[1] and Dawid Nidzworski[1]

[1] *Institute of Biotechnology and Molecular Medicine, 3 Trzy Lipy St., 80-172 Gdańsk, Poland*

[2] *Department of Metrology and Optoelectronics, Faculty of Electronics, Telecommunications and Informatics, Gdańsk University of Technology, 11/12 Gabriela Narutowicza St., 80-233 Gdańsk, Poland*

[3] *Institute of Microelectronics and Optoelectronics, Warsaw University of Technology, 75 Koszykowa St., 00-662 Warsaw, Poland*

[4] *The Centre for Plasma and Laser Engineering, The Szewalski Institute of Fluid-Flow Machinery, Polish Academy of Sciences, 14 Fiszera St., 80-231 Gdańsk, Poland*

ABSTRACT

Ochratoxin A (OTA) is a hazardous contaminant of a large variety of plant and animal originated food. Herein, we report an interaction of OTA with calf thymus DNA (ct DNA) on the nanodiamond surface. We employed multispectroscopic techniques to elucidate the binding mechanism of OTA with ct DNA. The fluorescence and UV-Vis spectroscopy results show that OTA binds to ds ct DNA and forms complexes.

We obtained the binding constants of OTA and ct DNA using fluorescence quenching and UV-Vis spectroscopy. The binding constant (K_b) for the interaction of OTA with ct DNA was determined using spectroscopic methods and was determined as 3.27×10^5 M^{-1} (UV-Vis) and 8.12×10^5 M^{-1} (fluorescence) for nanodiamond in green tea beverage OTA. Performed analyses directly indicate that OTA can interact with calf thymus DNA in a groove-binding mode as proved by the hyperchromic effect of the absorption spectra. This study of OTA–ct DNA interaction may provide novel insights into the toxicological effect of the mycotoxins.

KEYWORDS: fluorescence; nitrogen-vacancy nanodiamonds; ochratoxin A, calf thymus DNA; UV-Vis spectroscopy;

1. Introduction

Mycotoxins are naturally occurring toxins produced by certain mold species. The main fungal genera producing the mycotoxins include *Aspergillus*, *Fusarium*, and *Penicillium*. The most common mycotoxins are aflatoxins, OTA, fumonisins, deoxynivalenol, T-2 toxin, and zearalenone [1]. The mycotoxins are present at all stages of the food chain and can be found in products such as meat, fruits, wine, beer, coffee, tea, milk, nuts, dried fruits, cereals, and many more. Additionally, these compounds exhibit high chemical stability. Their crystallization state and high resistance to high temperatures or even gamma radiation [2] make them insensitive to conventional sterilization methods. On the other hand, chemical products that are able to neutralize their toxic effect are often causing other health problems.

Among the mycotoxins listed above, OTA is recognized as one of the most toxic and has been classified as a group I carcinogen. Although the toxicity of OTA has been studied for many years, its complex mechanism of action has not been elucidated in detail yet. However, based on *in vitro* and animal studies, this toxin is *'this time was* as carcinogenic, teratogenic, hepatotoxic, neurotoxic, and immunotoxic.

OTA is also known to generate covalent DNA adducts and to promote oxidative DNA damage based on the production of reactive oxygen species [3]. DNA is of key importance in the molecular processes of all living organisms. Therefore, exploring the OTA–DNA interaction mechanisms is of great importance—first, to understand the exact DNA damage mechanism, and second, to develop the therapeutic drugs in the future. Throughout the years, DNA has been reported as a target molecule of various drugs and toxic compounds, which can lead to a change in DNA structures and genetic mutations. Molecules can interact with DNA in three different ways. First, through the intercalation between the DNA base pairs, which is the most effective and thus destructive one; second, through the groove binding; and the last one, through the electrostatic interactions.

To study the interaction mechanisms of small molecules with DNA, several techniques have been utilized and reported, i.a. fluorescence spectroscopy [4], UV-spectrophotometry [5], circular dichroism [6], mass spectrometry [7], molecular docking [5], and electrochemical methods [6]. Moreover, techniques like competitive displacement, iodide quenching effect, viscosity measurements, and DNA melting assays have been used for further identification of the binding mode.

According to the literature, the mycotoxins have already been grafted on a few different surfaces. [8]. In our experiment, we used a nanodiamond surface with COOH functional groups, previously studied by Tian *et al.* [9]. The surface coverage, according to *ab-initio* calculations for COOH presented in [9], is approximately 6%. The carboxylated nanodiamonds (NDs) are efficient fluorescent agents enabling grafting various surface species [10] or interacting with biomatter [11]. The fields of physics and biology have discovered nanodiamond as an ideal material for at least two very different scientific applications. Biologists, on the one hand, have found that diamond nanoparticles show promise as exceptionally robust fluorescent dyes, with many potential applications in biolabeling [12,13]. On the other hand,

physicists have made tremendous progress in understanding and controlling the electronic properties of vacancy [12,14]. Before introducing the nitrogen-vacancy (NV) center in nanodiamond and its use for nanoscale sensing, we note that several excellent reviews have appeared highlighting different aspects of diamond nanoparticles and NV centers. Jelezko & Wrachtrup [15] have given an early overview of NV centers in diamond. More detailed descriptions of photoelectric detection and quantum readout of the NV center have been given by Bourgeois et al. [16]. Chi-Cheng Fu et al. [17] have provided an overview of the nanodiamonds as fluorescent cellular biomarkers.

NV centers in the nanodiamonds are atomic-level defects which display a remarkable range of properties, including sustained fluorescence, long quantum coherence times under ambient conditions, and demonstrated biocompatibility [18–20]. The nanodiamonds containing negatively charged NV centers have proven to be a promising tool in bio labeling, biomarking [21]. Recently, an important element of nanodiamonds has been surface functionalization [22].

In this work, we have explored interactions between calf thymus DNA (ct DNA) and OTA grafted at the fluorescent nanodiamond's surface. To date, fluorescent nanodiamonds have been used only as a sorbent / carrier of the mycotoxins to facilitate their removal from an organism and to neutralize their toxic effect [23,24]. Thanks to NDs tailored chemistry, OTA has been immobilized stably on the NDs' surface during experiment conduction. The OTA immobilization density and stability were also revealed by *ab-initio* simulations at the diamond [111] surface covered with 6% of carboxyl linkers.

Furthermore, the immobilization of OTA has been performed in a few, widely available drinks, beverages, and liquids to assess the influence of the environment on OTA toxicity. What is more, complex of the OTA and NDs enables the investigations of the DNA-OTA interactions using both fluorescence and UV-Vis spectroscopy.

2. Experimental

2.1. Materials

Carboxylated, fluorescent nanodiamonds with an average size of 750 nm, purchased from Adámas Nanotechnologies, USA have been chosen as substrates for immobilization of OTA. The Ochratoxin A from *Aspergillus ochraceus* has been received from Sigma-Aldrich, Poland. The stock solution of ct DNA has been obtained from Sigma Aldrich, Poland

Both OTA and ct DNA have been stored in phosphate buffer saline (PBS; pH=7.4) containing 140 mM of sodium chloride (NaCl), 2.7 mM of potassium chloride (KCl), 0.1 mM of sodium phosphate dibasic (Na_2HPO_4), and 1.8 mM of potassium phosphate monobasic (KH_2PO_4), all of which have been supplied by Sigma-Aldrich, Poland. OTA was suspended in PBS at 1 mg/mL concentration and stored as aliquots at -20°C. The ct DNA has been suspended in 0.01 M PBS, and its concentration was determined using UV-Vis spectroscopy based on the UV absorbance measurement at 260 nm using a molar extinction coefficient of 6600 $M^{-1}cm^{-1}$.

For immobilization of OTA on the nanodiamonds' surfaces, the following chemicals have been selected: 4-aminophenylacetic acid, N-hydroxysuccinimide (NHS), 1-ethyl-3-(3-dimethylaminopropyl)-carbodiimidehydrochloride (EDC), potassium ferricyanide ($K_3[Fe(CN)_6]$), potassium ferrocyanide ($K_4[Fe(CN)_6]$), dimethylsulfoxide (DMSO), sulfuric acid (H_2SO_4) (98%), and ethanol (98%). All of the chemicals listed above have been supplied by Sigma-Aldrich, Poland.

For the assessment of an impact of a liquid environment on OTA's interaction with ct DNA, the following comestibles have been selected: 10% spirit vinegar, 100% lemon juice, 100% apple juice, and green tea. Deionized water has been used as a reference. Detailed information on pH, and the origins of the comestible liquids is summarized in **Table 1**.

Table 1. Origins, and values of pH of the comestible liquids used in the experiment.

Comestible liquid	pH	Manufacturer
Spirit vinegar, 10%	2.38	OCTIM Sp. z o.o., Poland
Lemon juice, 100%	2.55	Polenghi LAS s.r.l., Italy
Apple juice, 100%	3.51	Tymbark - MWS Sp. z o.o. Sp.k., Poland
Green tea	7.10	Unilever Polska Sp. z o.o., Poland

2.2. Experimental Procedure

The nanodiamonds were separately suspended in every one of the 4 comestible liquids, and in deionized water. A concentration of the diamond in the suspensions was 0.1% (w/w). To ensure a repeatability of the samples, the following procedure for the tea brewing has been established: one sachet bag of the green tea was poured with 250 mL of filtered, boiling water, and removed after exactly 5 minutes. Before OTA was immobilized on the nanodiamonds' surfaces, the suspensions were being homogenized in an ultrasonic bath (Polsonic Sonic-3, 40 kHz) for 30 min.

In the present study, OTA was directly immobilized to 4-carboxymethylaniline (CMA). The proposed reaction scheme (**Figure 1**) consists of an activation of carboxyl groups on OTA with EDC/NHS, and a crosslinking of the activated carboxyl groups to amine groups generated on CMA-coated nanodiamonds' surfaces. First, 10 mg of 4-carboxymethylaniline (CMA) were activated in the presence of 20.5 mg of EDC, and 11.5 mg of NHS in 1 mL of PBS for 30 min with stirring. After the activation, carboxylic acid terminal moieties of CMA were converted to amine groups during incubation with 1 M ethylenediamine (EDA), pH 8.5 for 7 min. Free carboxylic groups were blocked with 1 M ethanolamine (EOA), pH 8.5, during incubation lasting 2 min.

After OTA was attached to the surfaces of the nanodiamonds, its interaction with ct DNA was investigated by means of UV-Vis spectroscopy, fluorescence spectroscopy, and analysis of zeta potential.

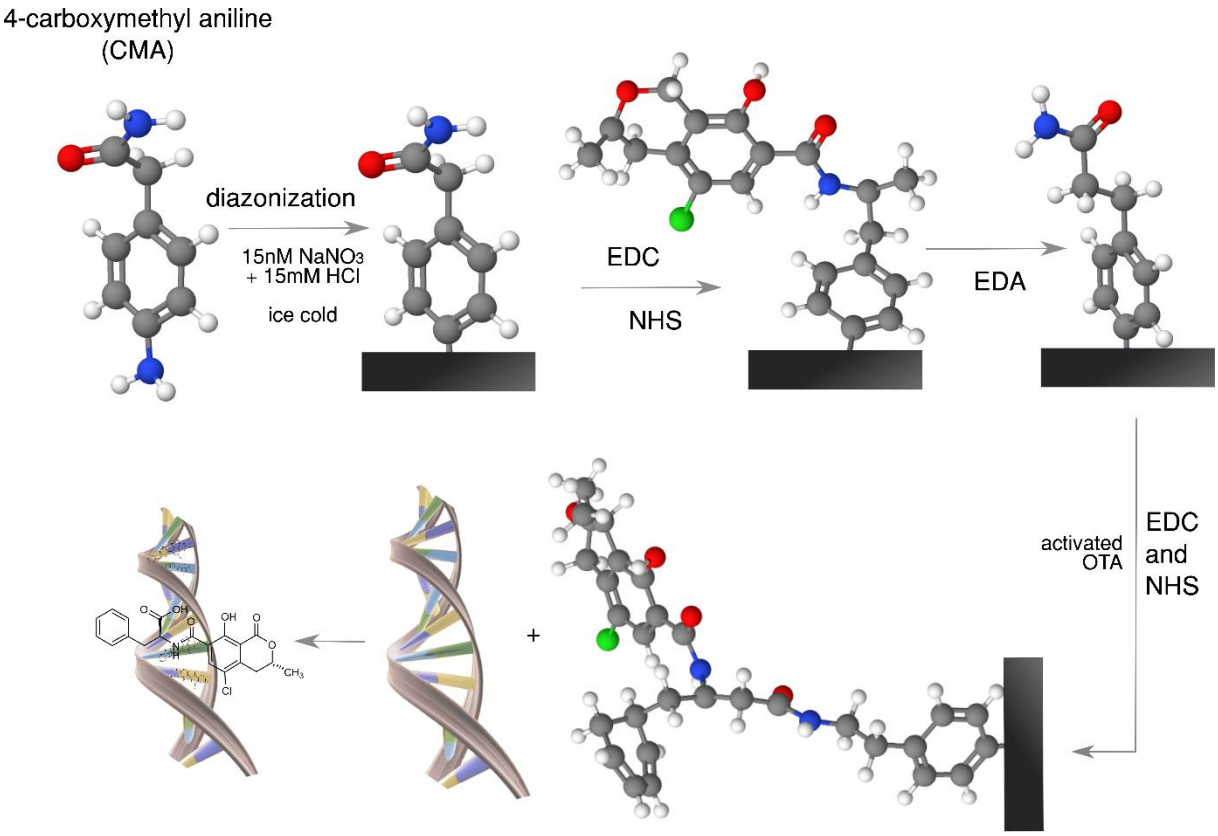

Figure 1. Scheme of nanodiamond modification by OTA and graphical representation of DNA-OTA interactions.

2.3. Apparatus

A high-precision quartz glass cuvette with outer dimensions of 45 × 12.5 × 12.5 mm and an optical path length of 10 mm has been used to analyze the UV-Vis absorption, and the fluorescence of the samples. All the absorption spectra were recorded in 250–650-nm range with the Perkin Elmer Lambda 35 UV–Vis spectrometer equipped with the integrating sphere module for reflectance measurements.

The fluorescence spectra were measured using a custom-made setup with 532 nm CW Nd:YAG SHG laser (Millenia, Spectra Physics) as an excitation source. The spectra were analyzed using 0.3 m monochromator (SR303i, Andor) equipped with 600 groves/mm grating and recorded with ICCD detector (DH740, Andor). The samples were excited by the laser from the front at 45° angle. The fluorescence signal was collected using the quartz lens end focused on the entrance of optical fiber. In the detection path the band-pass filter (OG570, Schott) was used to block the laser radiation.

The electrical properties (conductivity and zeta potential) of the samples were measured using the Zetasizer Nano ZS (Malvern Panalytical, UK) particle analyzer equipped with a high concentration cell.

2.4. Measurement Procedures

In the analysis of both the UV-Vis absorption, and the fluorescence, an empty cuvette was measured first to register a background signal, which would later be subtracted from the spectra of the samples.

Next, 2 mL of the suspension of OTA-immobilized nanodiamonds were placed in the cuvette and analyzed. Then, the suspension of ct DNA was added portion-wise to the suspension present in the cuvette. The following volumes of ct DNA suspension in total were added to the cuvette: 20 µL, 40 µL, 60 µL, 80 µL, 100 µL, 150 µL, 200 µL, 500 µL. After each portion of the ct DNA suspension was added, the sample was vortexed (VELP Scientifica TX4) for 10 sec at 400 rpm, and then left for 5 minutes, after which the absorption and fluorescence measurements were carried out.

The conductivity and the zeta potential of the samples were examined at 25°C at three stages of modification of the nanodiamonds: after the nonmodified nanodiamonds were dispersed in the liquids in 0.1% concentration; after OTA was immobilized on their surfaces; and finally after the addition of 500 µL of the solvent containing ds ct DNA to 2 mL of the suspensions of the OTA-modified nanodiamonds.

2.5 Ab-initio and Molecular Dynamics Simulation of ND-OTA Complexes

The *ab-initio* simulations were conducted on the [111] oriented diamond slab containing 4950 carbon atoms (9 layers, each containing 550 atoms). Model was created using the Atomistix Tool Kit Quantumwise [25] (ATK, Synopsys, USA). The diamond slab was terminated by COOH groups with covalently grafted OTA. The thickness of the slab was 19.6 Å. The model is assumed to be an infinite plane; on the borders of supercell the periodic boundary conditions were applied. To leave sufficiently large space for the adsorbing molecules and analyze interaction with images, the 6.8 nm vacuum buffer was added above the surface. Periodic boundary conditions were applied in the unit cell, while the ratios between atom types within the cell were kept similar for the entire surface.

The [111] diamond surface consists of 225 surficial carbon atoms, where each of the carbon atoms forms three bonds with other carbons. Priorly, hydrogen atoms are bonded to each carbon atom resulting in the 100% hydrogen termination. If the single hydrogen atom is removed, the surface gets radical site (per unit cell). Radical site could be saturated by the COOH (or OTA), then the percental coverage changes to $1/225 \approx 0.44\%$. Surface coverage is usually estimated in reference to all possible radical sites on the given surface, regardless the occupation. Such a convention was already used in the papers describing surface chemistry simulations [9]. Large molecules such as OTA could cover up the diamond surface which is already covered by relatively small atoms such as H enabling the intersection of the covered areas. This phenomenon does not impact the percentage coverage, which is independent of the molecule geometrical size. Models used in Force-Field and density-functional theory (DFT) calculations have different cell sizes but similar percentage coverages of COOH and OTA. During all Force-Field calculations on the diamond surface, 13 COOH species were present corresponding to 5.77% coverage.

The applied ochratoxin structure was downloaded from the PubChem [26] databases (CID 442530). The binding to the diamond surface was conducted to reproduce the mechanism presented in **Figure 1**. Six

separated slabs were designed containing perpetually increased number of OTA molecules bounded to diamond surface, from one to six per chosen area (see **Figure 2)**. The binding energy E_{bind} of the model system can be calculated using the formula (1).

$$E_{bind} = \frac{1}{n}(E_{slab+OTA} - E_{slab} - nE_{OTA}) \quad (1)$$

Where $E_{slab+OTA}$ is the total energy of the system with OTA and all terminating species, E_{slab} is the energy of the system without OTA (the radical sites created by removing OTA are left passivated), and E_{OTA} is the energy of one isolated OTA species. Small *n* denotes the number of OTA molecules in the supercell.

To describe the energy of the system, the ATK Force-Field has been used. This module describes the interatomic integration using the classical potentials set. This implementation is described elsewhere [27]. To calculate the operating forces, the reactive force field ReaxFF_CHONSMgPNaCuCl_2018_08 was used [28]. Before the total energy calculation, the atomic positions and the cell size were optimized based on the Broyden-Fletcher-Goldfarb-Shanno (LBFGS) algorithm. The maximal force in the structure after optimization did not exceed 0.05 eV/ Å.

The diamond slab containing single OTA was applied for *ab-initio* band structure simulations by means of DFT. The Quantum ATK toolbox enables conduction of such calculations based on a couple of variants. The Linear Combination of Atomic Orbitals [29] (LCAO) was used to calculate electron density functionals. To solve the matrix equations of the LCAO method, self-consistent field (SCF) iterations were performed. The density mesh cut-off energy was set to 125 Hartree and k-point sampling utilizing MonkhorstPack scheme was 3x2x1. During DFT calculation, the exchange-correlation of electrons was included using GGA method with PBE (Perdew, Burke and Ernzerhof) functionals. The PseudoDojo [30] pseudopotentials with medium basis set were utilized to calculate the electron wave functions. The detailed description of the mentioned basis set can be found in the paper of Smidstrup *et al.* (appendix) [31].

3. Results and Discussion

3.1. Simulations of the Adsorption Energy Dependence on the Surface Coverage

The series of numerical studies were carried out to estimate the dependence of OTA adsorption energy on the ND surface. The key aspect of this calculation was to estimate energetically favorable OTA coverage density. The OTA coverage density and adsorption energies are plotted in **Figure 2**.

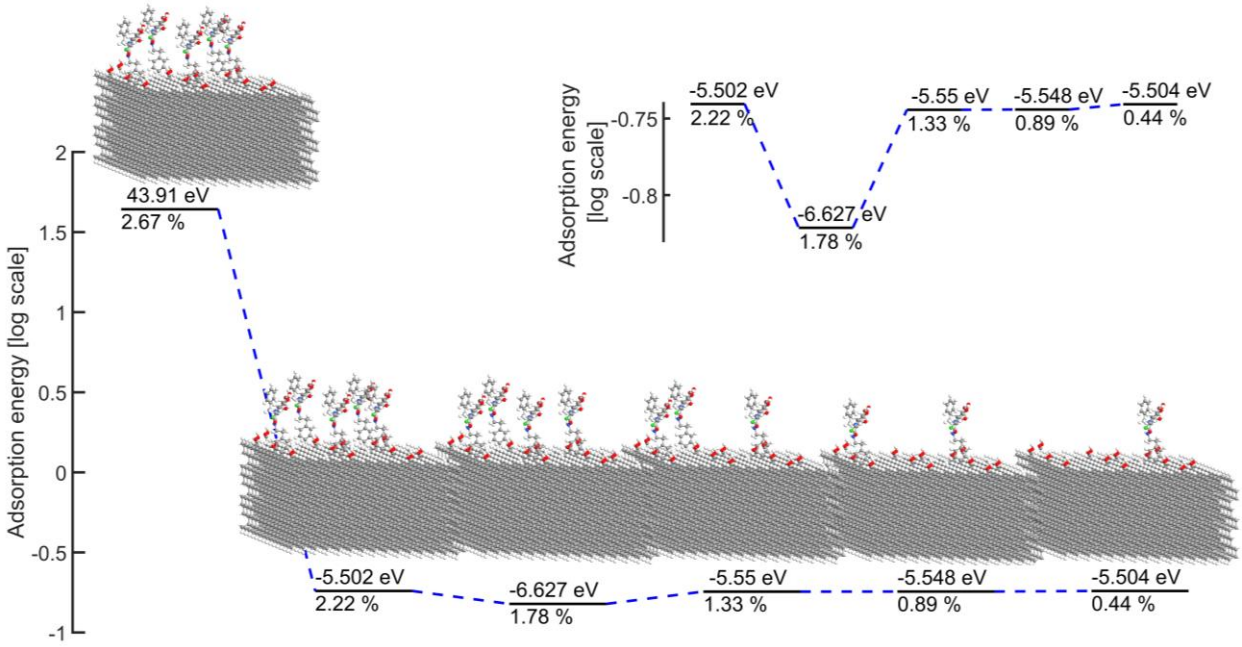

Figure 2. The binding energy for a series of [111] diamond models with different OTA concentration on the surface.

According to Force-Field calculation, the energetically favorable OTA surface coverage is equal to 1.78%, exhibiting the lowest energy. The adsorption energy at this coverage is -6.627 eV per adsorbed ochratoxin molecule. The adsorption energy per each molecule for low concentration decreases monotonically with increasing percentage of coverage. This phenomenon could be attributed to the stabilization of the long-range interactions between the adsorbed OTA molecules [32]. The well-known fact is that the significantly different energies are associated with various conformation of the organic molecules [33]. Once the percental surface coverage exceeds the limiting value, the distance between molecules is as low as the cross-linking and bond breaking processes starts to occur [9]. The initialization of the breakdown leads to the massive surface recombination which is associated with the desorption of OTA molecules. Such a process is indicated by the rapid increase of the adsorption energy. The competitive influence of mentioned processes will push the system to preserve the OTA concentration at the level close to optimal energetically stable.

3.2. Ab-initio Simulations of ND-OTA Complex

The diamond slab containing single OTA molecule was utilized to simulate *ab-initio* band structure of the studied ND-OTA complex by means of DFT. The horizontal size of the slab was aligned to set the OTA coverage to 1.78%. The coverage of COOH was kept at 6.66%. The slab is displayed in **Figure 3a**. Additionally, the reference, H-terminated diamond slab, covered only by COOH (see **Figure 3c**), has been created. **Figures 3b,d** display projected band structure based on the *ab-initio* simulations. This

type of the band structure includes the projection of a state on a specific group of atoms, in this case OTA and COOH.

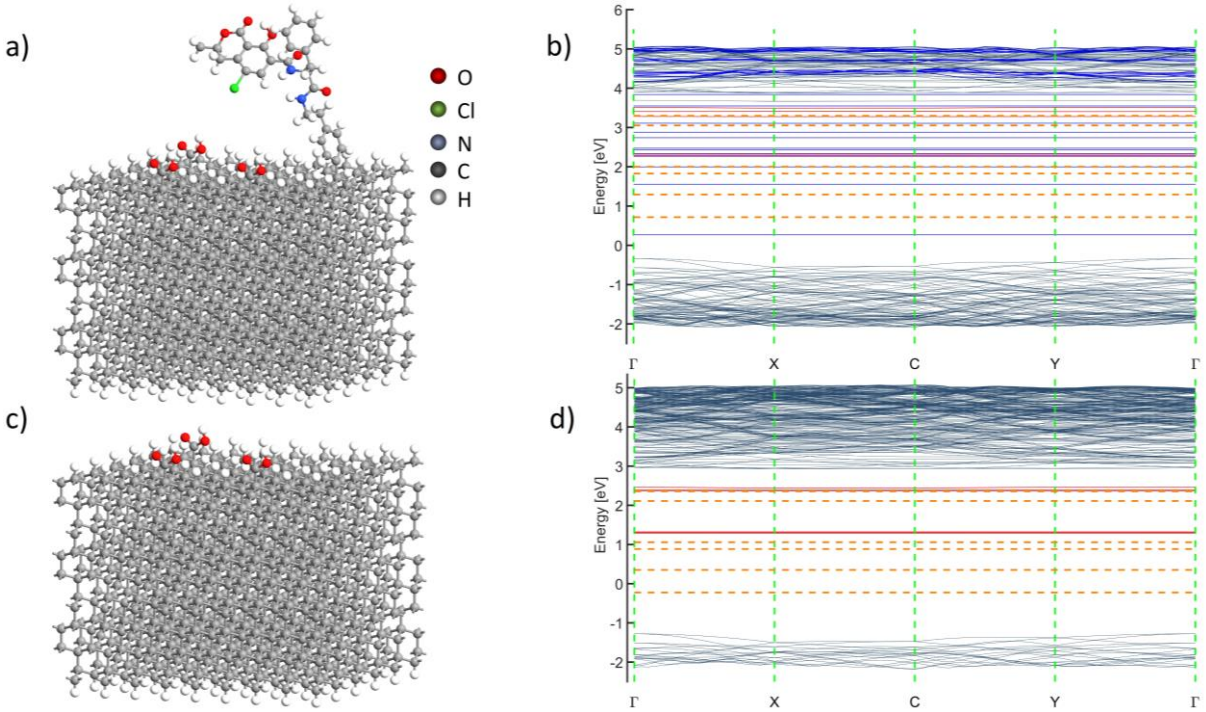

Figure 3. **a)** The model of diamond [111] surfaces with adsorbed ochratoxin; **b)** Projected band structure of the ND-OTA complex; **c)** Reference model of the slab terminated by the mixture of COOH and H; **d)** Projected band structure of the slab presented in d, red states were introduced by adsorbed molecules. (Attn. The blue states were introduced by OTA, red by COOH, orange dashed lines indicate position of states of NV^- defects as calculated previously [34] while black states are associated with the diamond slab).

In this work, the interaction of the adsorbed OTA molecules with NV^- color centers is particularly investigated. The energy states of NV^- center were extensively studied up to now [34–37]. Here,the available literature data [34–37] has been applied instead of calculating the position of the NV states. The band gap of diamond as shown in **Figures 3b,d** (orange dashed lines).

The presented projected band structure data clearly shows that adsorption of both COOH and OTA introduces the electron states in the band gap of the diamond. In the case of COOH functionalization new energy band is introduced below the lower conduction band. As an effect, the band gap shrinks by the 40% relative to the hydrogen-terminated surface bandgap. A similar effect, however at higher concentration of carboxyl, was predicted on the ground of ab-into simulation of nanodiamond cluster electronic properties [38]. Introduction of the OTA functionalization results in further shrinking of the fundamental band gap, divided both by introduction of OTA energy levels into fundamental band gap of diamond and upshift of the valence band. As an effect of combined processes, the bandgap width shrinks by 84% in comparison to the hydrogen-terminated [111] diamond surface.

The introduction of the surface states by the adsorbent species is well-known, but in these particular conditions the most important is the location of these states in the energy-momentum space. The states residues in the region close to the states introduced by the NV^- centers. The overlapping of surface termination states is particularly evident in **Figure 3b**, which presents the band structure of [111] diamond surfaces covered by both COOH and OTA. Several states are positioned within the NV^- bandgap, implying the strong interactions between ND-NV and OTA, which could even deactivate the NV fluorescence [34,39].

To get qualitative measure of influence of OTA functionalization effect on the electronic properties, the work function (WF) calculations were conducted. Both band structure and WF were simulated using similar model as shown in **Figure 3**. The electron WF was calculated for different cases of surface functionalization. The fully hydrogenated surface results in WF of 4.83 eV being in agreement with prior experimental data [40,41] for [111] diamond. The partially hydrogen-terminated diamond functionalized with 6.66% of COOH groups (see **Figure 3c**) manifests WF equal to 6.21 eV. Finally, the adsorption of 1.78% OTA results in WF of 6.49 eV (see **Figure 3a**). Observed changes are in agreement with approach described in [42] where WF values could be recalculated to the electron affinities.

The hydrogen termination induces the formation of the positively-charged surface, causing band bending close to the diamond surface [43], thus NV centers will be favored to convert in the neutrally charged state. According to conducted DFT simulation, OTA-coated diamond [111] surface will exhibit positive electron affinity. This suggests that the surface will be negatively-charged.

Despite the relatively low concentrations of both COOH and OTA, the band structure of the ND-OTA complex was significantly distorted by the covalent adsorption of OTA. Qualitative analysis of the projected band structure and quantitative studies on the chemical potentials lead to the conclusion that binding of OTA to the nanodiamond surface should stabilize concentrations of the NV^- centers.

Spectroscopic experiments revealed the decay in the fluorescence emission of the ND-OTA complexes in function of increased the ct DNA concentrations (**Figure 6**). The simulation results suggest that the light scattering and absorption or fluorescence quenching in the DNA-rich buffer are additional processes responsible for the observed decay effect.

3.3. Spectroscopic studies on the ND-OTA interactions with DNA

Phosphate chromophores and aromatic bases are the cause of the characteristic DNA absorption peak positioned at *ca.* 260 nm. The chromophore groups, namely purines—adenine and guanine—and pyrimidines—cytosine and thymine, are the cause of the given maximum absorption peak [44]. Thanks to this characteristic, one can utilize UV-Vis absorption measurement for the detection of various complex formations. This technique, taking into account its simplicity and effectiveness, enables the detection of various DNA–molecule interactions and the formation of new complexes. As the result of these spatial changes, the absorbance intensity in the UV-Vis range as well as the band position are altered. Bathochromism is observed during intercalation if the π* orbital of the intercalating molecule couples with the π orbital of the DNA base pairs, resulting in the decreased π* transition energy. However, the coupling π orbital is not fully saturated with electrons. To detect an interaction between DNA and a chosen molecule, one can observe the shift in the maximum position of this band before and after the addition of the ligand to the tested DNA solution.

UV–Vis is usually used as a standard technique to quantify the amount of DNA in a sample. DNA bases absorb strongly at 260 nm in an aqueous buffered solution at pH 7.4 [6]. The absorbance values obtained for this wavelength are used for the calculation of the DNA concentration and the stability analysis. OTA was dissolved in PBS, pH 7.4. In the present experiments, the addition of 10 μL of calf thymus DNA (ct DNA) to OTA strongly influenced the UV spectra. The absorption band intensity regularly decreased over time, which was also observed in many other studies [45],[46]. Usually, the time needed to establish the reaction equilibria was around 3–5 min [47]. In the present study, the overall time for the determination of equilibria was 3 min for ss ct DNA and 5 min for ds ct DNA (**Figure 4**). This time was accepted as optimal for the intercalation, to study the effects of OTA interactions with ct DNA [46].

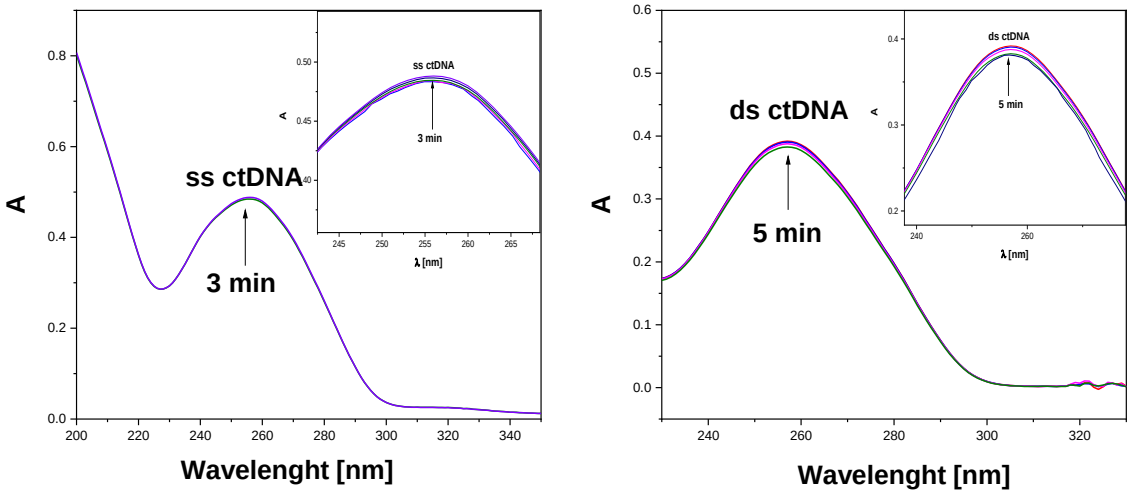

Figure 4. The influence of the incubation time on the band intensity of OTA (2×10^{-4} M) after addition of ct DNA, 10 µL (ss ct DNA and ds ct DNA) in aqueous phosphate buffer solution, pH 7.4.

The UV spectra of the ND-OTA suspensions with different concentrations of ct DNA were obtained. As shown in **Figure 5**, with increasing concentrations of ct DNA, the intrinsic binding constant K_b of OTA with ct DNA can be determined according to Benesi–Hildebrand equation:

$$\frac{A_0}{A - A_0} = \frac{\varepsilon_G}{\varepsilon_{H-G} - \varepsilon_G} + \frac{\varepsilon_G}{\varepsilon_{H-G} - \varepsilon_G} \times \frac{1}{K_b[DNA]}$$

where K_b is the binding constant, A_0 and A are the absorbance of the OTA and its complex with ct DNA, and $\varepsilon_{H\text{-}G}$ are the absorption coefficients of the OTA

Figure 5 shows the absorption spectra of OTA in the presence of the increasing amounts of ct DNA to decrease in the peak intensities. Intercalating binding commonly results in the hypochromic and bathochromic effect of the intercalated chromophore transition. The spectral changes observed in the form of 'hypochromism" effect during the process, reflect the change in conformation of DNA and structure of DNA. It has been reported in literature that hypochromism is due to the intercalative mode involving a strong stacking interaction between an aromatic chromophore of a molecules and base pairs of DNA. Generally, the external groove binding causes a slight spectral shift, a hyperchromic effect. In all the spectra obtained, we observed the band with the maximum absorption in 270 nm, but for 10% spirit vinegar we observed the maximum at 230 nm.

Furthermore, comparing with the K_b value of other DNA groove mycotoxin binders, the binding mode between OTA and the ct DNA was deduced as groove binding. The association constant can be obtained from the intercept-to-slope ratios of $A_0/(A - A_0)$ vs. 1/[DNA] plots. Based on the intersection-to-slope ratio, the greatest K_b value was calculated as 3.27 x 10^5 M^{-1} for the diamond suspended in the green tea

346 solution. The K_b binding constant values reported herein are higher than those typically found for the
347 well-known toxins (**Table 2**) such as Aflatoxin B1 ($K_b = 7.60\times10^4\ M^{-1}$) and Wortmannin ($K_b = 2.20\times10^4$
348 M^{-1}).
349

350 **Table 2.** Comparison of the binding parameters for various toxins–ct DNA interactions obtained using UV-Vis
351 spectroscopy.

Compound	Binding constant [M^{-1}]	References
Isoxazolcurcumin	1.15×10^4	[45]
Wortmannin	2.20×10^4	[48]
Farrerol	11.80×10^5	[49]
Aflatoxin B1	7.60×10^4	[50]

352
353
354
355
356

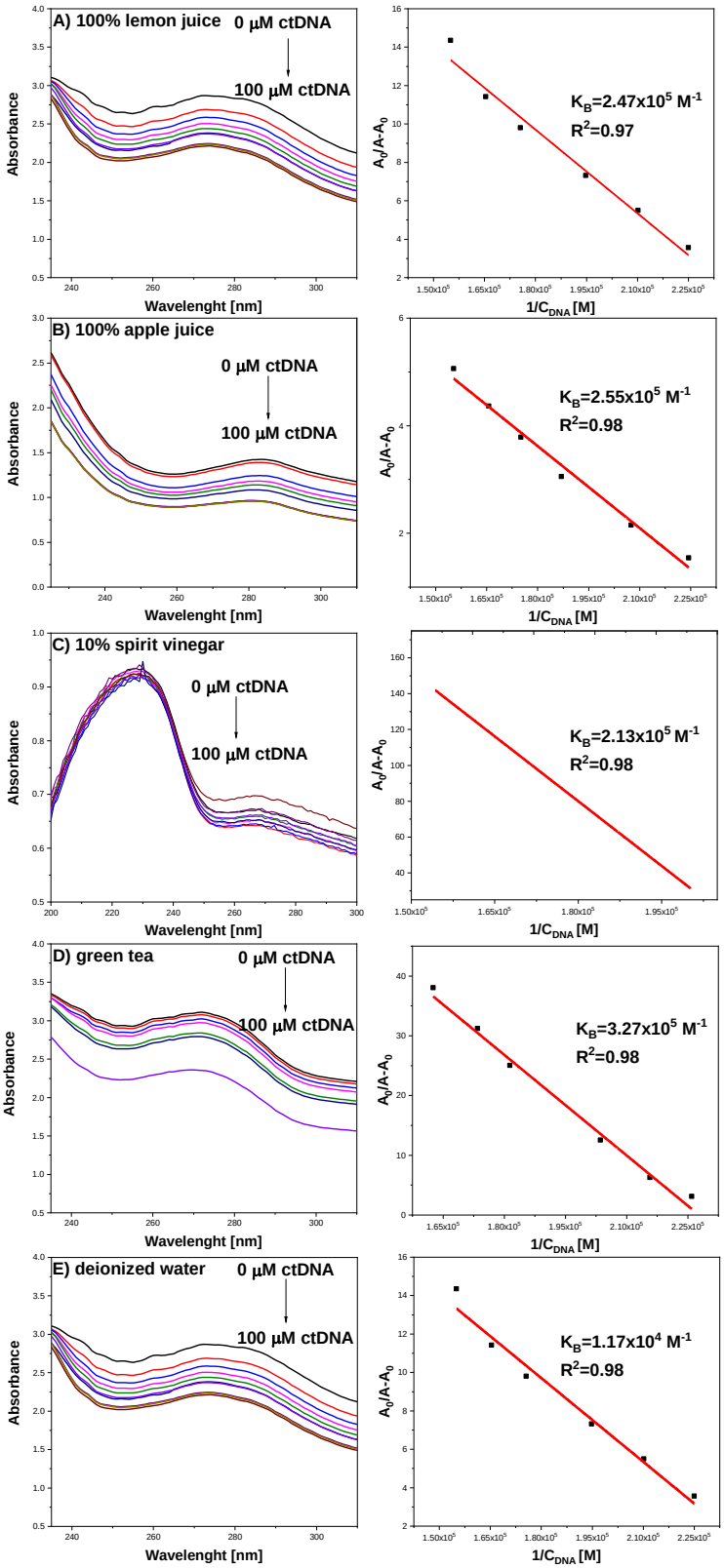

357

358 **Figure 5.** UV–Vis absorption spectra of OTA in different comestible liquids and plots of (A_0/(A-A_0)

359 versus 1/ [DNA].

3.4. Fluorescent Analysis of the ND-OTA complex with DNA

The fluorescence spectra were obtained for the whole suspension (solvent, diamonds, OTA, ct DNA) and were dominated by the fluorescence of diamonds which emit such intense radiation due to the nitrogen-vacancy (NV) fluorescent color centers contained therein (**Figure 6**). The fluorescence intensities decreased regularly with the increase of ct DNA concentration. The titration data were analyzed according to the Stern–Volmer equation and investigated on the interaction types of ct DNA with the five suspensions of the nanodiamonds. The fluorescent intensity significantly decreased with increasing concentration of ct DNA. Therefore, fluorescence data could be studied using the Stern–Volmer equation [51]:

$$\frac{F_0}{F_0 - F} = \frac{1}{f_a K_{SV}} \frac{1}{[ct\ DNA]} + \frac{1}{f_a}$$

where F_0 and F are the fluorescence intensities in the absence and presence of a quencher; f_a is the fraction of the accessible fluorescence; K_{SV} is the quenching rate constant of the biomolecules, and [ct DNA] is a concentration of calf thymus DNA.

To elaborate on the fluorescence exhibited by the nanodiamonds containing the NV centers, it is advisable to concentrate first on the analysis of the spectra registered for the reference suspension based on deionized water. This suspension was selected as it is least likely to alter the signal emitted by the particles. Local maxima at 575 nm and 637 nm are the zero–phonon lines (ZPLs) of NV^0 and NV^- centers, respectively [52]. The much higher intensity of the ZPL of the negatively–charged centers indicates their quantitative advantage over their electrically neutral counterparts. While the ZPL of NV^- centers is clearly visible in every fluorescence spectrum registered in the experiment, the ZPL of NV^0 centers is quenched by the liquid medium in the suspensions based on lemon juice, apple juice, and green tea. Broad peaks at 659 nm and 682 nm are the vibronic (phonon) sidebands of the NV^- centers [53] with the known energy shifts of 65 meV [54] and 63 meV [52], respectively. It is worth noting that the majority of the signal emitted by the NV^- centers falls to the phonon sidebands, and not the ZPL, which is a common occurrence when the measurements are carried out at room temperature [55].

In every fluorescence spectrum of the sample based on the lemon juice there is a very intensive, broad peak observed at 677 nm. This peak is a superposition of the 2nd phonon sideband of the NV^- centers, and the maximum already present in the signal emitted by the pure lemon juice. A broad peak at 585 nm registered for the suspensions based on the green tea comes from the dispersion medium itself. The same peak has been identified in the spectrum of pure green tea. Lin *et al.* [56] found that the emission intensity in the range of 500–600 nm varies significantly between various kinds of green tea.

The OTA–DNA binding mode can be determined by fluorescence spectroscopy and various analytical tools based on the fluorescence emission can also provide particularly useful information. Moreover, the effective interaction with DNA usually causes a significant change of the fluorescence intensity as a consequence of various factors. Representative spectra obtained for OTA in the absence and the presence of calf thymus DNA dissolved in the solution are shown in **Figure 6.** We observed that with the increasing DNA concentration, the emission spectra of OTA show remarkable distribution and hyperchromic effect.

Given that OTA could emit fluorescence under ultraviolet irradiation, a series of experiments based on the fluorescence spectroscopy were performed to explore the binding mechanism of mycotoxin to ct DNA. The fluorescence intensity of OTA–DNA complex is quenched upon the addition of ct DNA. OTA on the nanodiamond surface in lemon juice displayed strong emission spectra, with emission local maximum at 637 nm. After the addition of ct DNA in a small concentration to OTA solution, we observed that the position and shape of the peaks did not change. Thus, it can be assumed that OTA interacts with ds ct DNA through noncovalent bonds rather than covalent bonds [57]. The K_{SV} value of the OTA–DNA complex at 298 K in various nanodiamond suspensions is presented in **Table 3**. The highest value K_{sv} of the OTA–DNA complex was 8.12×10^5 M^{-1} on surfaces of nanodiamonds suspended in green tea. A comparison shows that the K_{sv} of the OTA–DNA complex on nanodiamonds using green tea solution was greater than in the case of other solutions. The difference in K_{sv} depends mainly on the structural differences of the solution. Green tea contains other compounds less analeptic than caffeine, xanthine derivatives, including theobromine, theanine, and theophylline which belong to the group of polyphenols [58,59]. This effect indicates that the hexatomic ring of OTA immobilized on nanodiamond suspended in green tea has a larger dimension and stronger stability than the other nanodiamonds, resulting in a stronger DNA binding.

416 **Table 3.** Binding constants for OTA–ct DNA interaction.

Nanodiamond suspensions	**Binding constant K_{sv} [M^{-1}]**
Lemon juice	2.25×10^5
Apple juice	2.43×10^5
Deionized water	7.10×10^4
Green tea	8.12×10^5
Vinegar	3.41×10^5

417

418

419

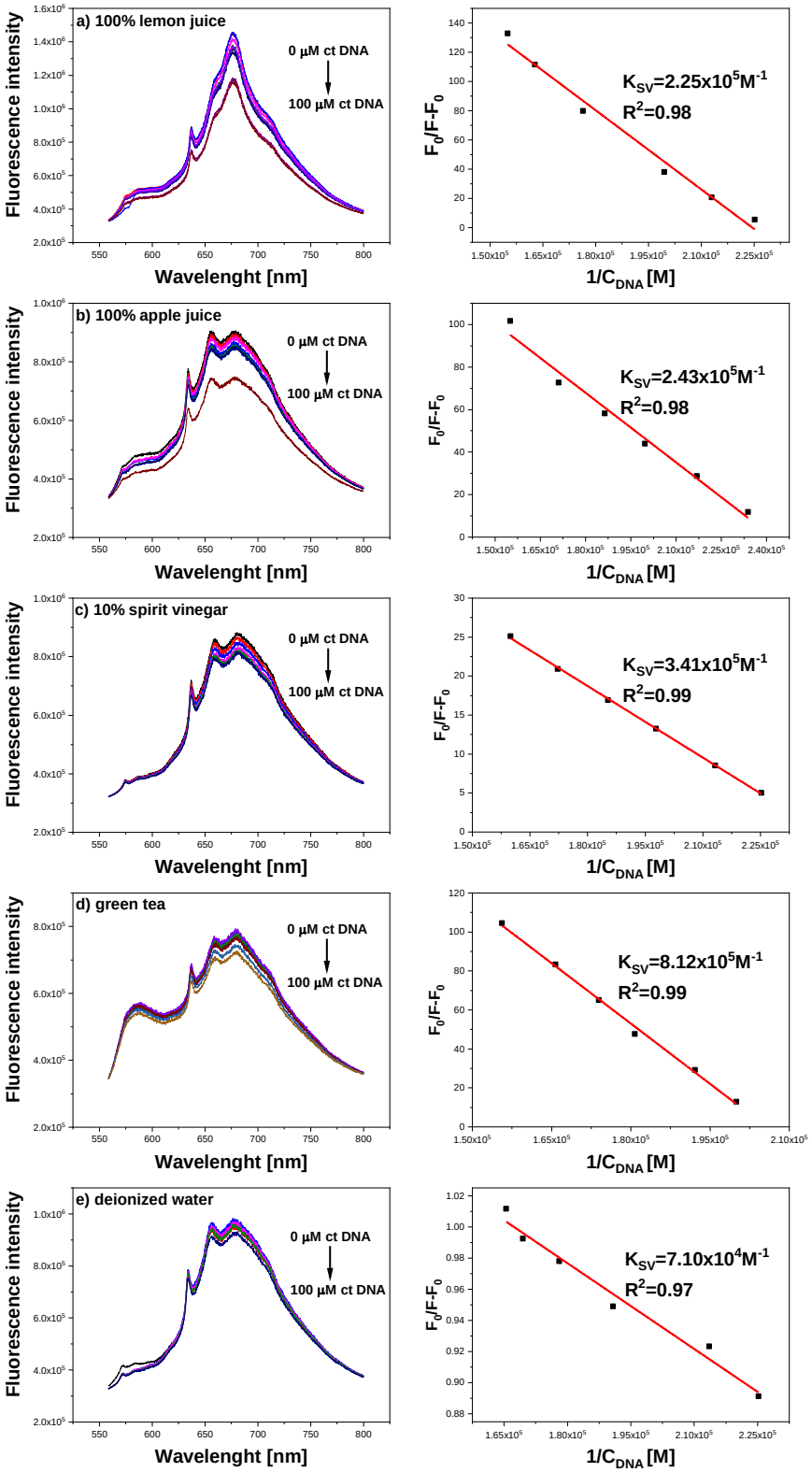

Figure 6. Fluorescence emission spectra of OTA–DNA system in various comestible liquids and plots of (F/(F_0-F) versus 1/ [DNA].

3.5. Analysis of the Particles Electric Potential

Zeta potential measurements were conducted to investigate the variation of the surface charge at each experimental step (**Figure 7a**). The carboxylated NDs, OTA-coated NDs, and OTA-coated NDs in the presence of the DNA in the sample have been investigated in comestible liquids, namely vinegar, lemon juice, apple juice, green tea, and deionized water. **Table 1** presents the pH values of the utilized liquids.

First, we measured the zeta potential of carboxylated NDs. At low pH values (lemon juice, apple juice, and vinegar) the zeta potential oscillates around 0 mV, reaching a minimum value of ~ -5 mV for the apple juice. This behavior is attributed to a large amount of mobile H^+ ions present in these suspensions, making the oxidized NDs' surfaces electroneutral, thus, unstable and prone to aggregation.

With the increase in pH, the zeta potential is decreasing, reaching the values of -20 and -43 mV for the green tea and water, respectively. Once the pH increases, H^+ ions become depleted from the solution as well as from the carboxyl groups present on the NDs' surfaces, generating the negatively charged particles and, therefore, stabilizing them in the solutions [60].

Next, OTA-coated NDs were measured. OTA contains phenolic and carboxylic groups (**Figure 9**), and therefore can exist in different ionization states: carboxy ionized (COO^-), phenolic ionized (ArO-), dianionic form (both carboxylic and phenolic ionized), depending on the local pH. The reported pKa values of the carboxyl group and the phenolic group of OTA are in the range of 4.2–4.4 and 7.0–7.3, respectively [61]. Furthermore, knowing that the OTA's carboxyl group is involved in the covalent surface functionalization, the only part which can be ionized is the phenolic group. For this reason, ND-OTA complexes in acidic environments stay electroneutral and prone to aggregation as OTA exists in this condition in a neutral state.

However, in the case of water and green tea, considering their pH, both forms of OTA are simultaneously present in various ratios in these solutions (neutral and anionic form). Thus, for instance, in the case of water, we observed slight neutralization of the negative charge and an increase in zeta potential from -43 to -38 mV. In the case of green tea, we did not observe any changes, which can be caused by the involvement of two forms of OTA on the ND surface. Consequently, the final effect may be an average of these two. Another reason may be the influence of the co-existing green tea ingredients. Green tea contains as many as 200 bioactive compounds, such as polyphenols, caffeine, theanine, which also can neutralize OTA influence.

The last and the most complicated case was OTA-coated ND in the presence of ct DNA. There are many factors involved in the interaction of a compound with DNA, such as temperature, ionic strength, or

temperature. The picture is even more complicated if the compound—in our work OTA—exists in more than one form in the solution, as each form interacts with DNA differently. In general, DNA is a negative polymer, hence this molecule exhibits higher interactions with cationic species than the neutral species. On the other hand, these interactions are greater than in case of species that are negatively charged.

Zeta potential measurements in acidic liquids revealed no observable changes, although a neutral form of the OTA may bind the DNA. However, DNA can change its 3D structure in highly acidic environments, starting from an elongated coil state to a compact one, what is closely related to its charge neutralization [62]. Also, DNA may partially denature in such an extreme condition, as a result making the interaction of DNA with OTA impossible in both cases.

In the case of water, as mentioned before, neutral and anionic form of OTA are present on its surface, while DNA will exist in an elongated structure with a negative charge. Therefore, the interaction between OTA and DNA may be somehow impeded. However, as reported by Saha *et al.* [63], the presence of the DNA in the examined sample can change the pKa value of the binding compound, in our case OTA immobilized on NDs' surface [63] and thereby changing the zeta potential of the surface. Another reason for the increase of the zeta potential value from -38 to -34 mV is the interaction (groove binding, or intercalation) of OTA with DNA, thus, neutralizing the negative charge of added DNA, as well as anionic phenolic group of OTA.

In the case of green tea, again, we did not observe any noticeable changes in the zeta potential. This effect can be justified by the same arguments as previously. In water, both forms of OTA are present; the pKa value of OTA can vary because of the DNA presence; interaction of OTA with DNA also may take place, however, the net charge may be neutralized by co-existing green tea ingredients.

The conductivities of the nanodiamond suspensions at different stages of the particles modification are presented in **Figure 7b**. The deionized water is the only dispersion medium that exhibits virtually no electrical conductivity with suspended unmodified nanodiamonds. At the same stage, every other sample shows initial conductivity, with the suspension based on the lemon juice revealing the highest value, followed by the sample based on the apple juice, then on the vinegar, and finally on the green tea. This relation among the conductivities of the suspensions is preserved at every stage of the modification of the nanodiamonds. The attachment of the OTA to the surfaces of the diamond particles, as well as the addition of double-stranded ct DNA to the suspensions, increase the overall conductivities of the samples.

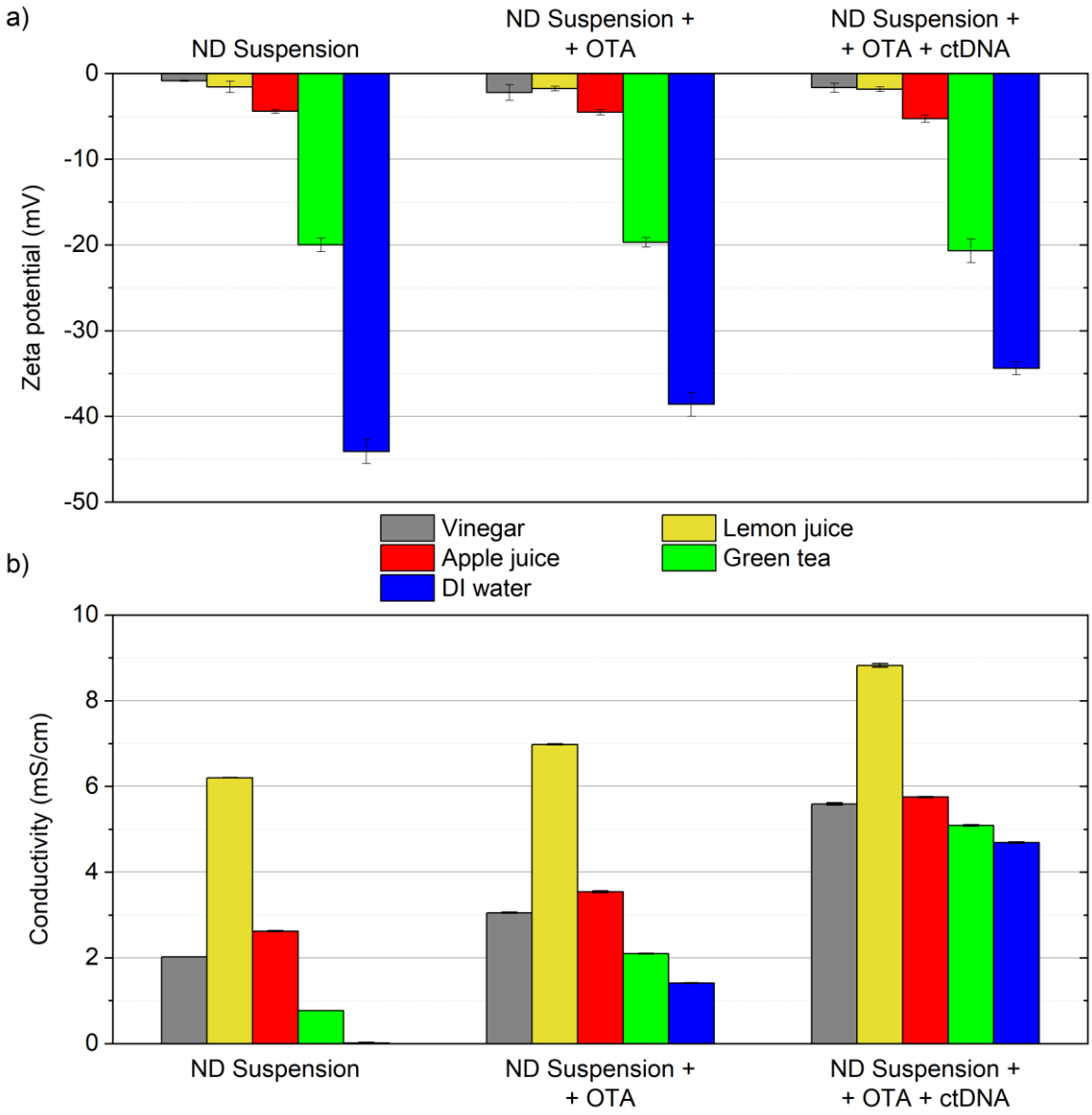

Figure 7. The electrical properties of the nanodiamond suspensions based on the comestible liquids; "ND Suspension" – the suspensions of unmodified nanodiamonds (0.1% concentration); "ND Suspension + OTA" – the suspensions of the nanodiamonds with OTA attached to the surfaces of the particles; "ND Suspension + OTA + ct DNA" – mixtures containing 2 mL of the nanodiamond suspensions with OTA attached to the surfaces of the particles and 0.5 mL of the solvent containing ds ct DNA; a) zeta potential; b) conductivity.

3.6. Effects of Mycotoxins on the Characteristics of the Denatured DNA

A difference was observed in the quenching effect of single-stranded DNA (ssDNA) and double-stranded DNA (dsDNA) when molecules were bound to DNA based on different interaction modes. In the groove bounding mode, the quenching interactions of dsDNA should be stronger than for

ssDNA. Weaker quenching effects of dsDNA comparing with ssDNA also slightly differed if small molecules intercalated between the DNA base pairs. The double strands were denatured. The quenching effects of both ssDNA and dsDNA also slightly differed if small molecules interacted with the phosphates groups of DNA based on electrostatic interactions [64–66]. The fluorescence quenching plots of OTA upon the addition of different concentrations of dsDNA and ssDNA are shown in **Figure 8.** The dsDNA exhibited a greater slope than ssDNA in OTA.

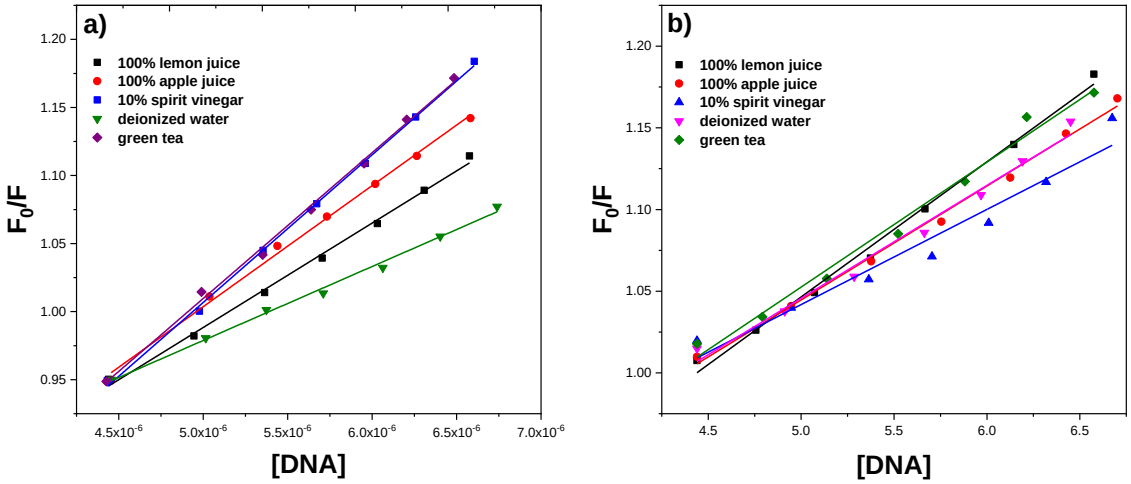

Figure 8. Fluorescence quenching plots of OTA for a) single-stranded DNA (ssDNA) and b) double-stranded DNA (dsDNA) in different comestible liquids in, $C_{OTA} = 2\times10^{-3}$M. F_0 is the fluorescence intensity of OTA and F is the fluorescence intensity of OTA for the various ssDNA and dsDNA concentrations.

Conclusions

In summary, the interactions of ND-OTA complexes with ct DNA were investigated using spectroscopic methods applying nitrogen-vacancy rich nanodiamonds suspensions. The characteristics of the interaction between OTA and ct DNA were studied in different comestible liquids The fluorescent measurements demonstrated that the intensity of the fluorescence significantly decreased with the increasing concentration of ct DNA. The UV-Vis studies indicated that the increasing concentrations of ct DNA lead to a decrease in the peak intensities.

We obtained the binding constants and the binding site sizes (0.97) of OTA with ct DNA at room temperature. Moreover, we managed to form a complex with ct DNA where a part of OTA occupies a space within the groove binding and the rest slips in between the stacked base pairs of duplex DNA via the intercalation mode of binding.

The presence of the adsorbed species introduces additional states to the fundamental diamond bandgap. The energy states of NV^- center lies near the states introduced by the adsorbed ochratoxin. Importantly, the states introduced by OTA lie in the bandgap of NV^- center lowering its width and changing the optical absorption and emission spectrum of the center.

The present study provides detailed information on the binding affinity, the mode of binding interaction, the main forces of OTA–ct DNA interactions, and the structure of OTA–DNA complex, which enables the further elucidation of the DNA degradation mechanism.

Acknowledgments

This work was supported by the TEAM-NET program of the Foundation for Polish Science co-financed by the European Union under the European Regional Development Fund QUNNA POIR.04.04.00-00-1644 /18.

Bibliography:

(1) Zheng, M. Z.; Richard, J. L.; Binder, J. A Review of Rapid Methods for the Analysis of Mycotoxins. *Mycopathologia* **2006**, *161* (5), 261–273. https://doi.org/10.1007/s11046-006-0215-6.

(2) Calado, T.; Fernández-Cruz, M. L.; Cabo Verde, S.; Venâncio, A.; Abrunhosa, L. Gamma Irradiation Effects on Ochratoxin A: Degradation, Cytotoxicity and Application in Food. *Food Chemistry* **2018**, *240*, 463–471. https://doi.org/10.1016/j.foodchem.2017.07.136.

(3) Mally, A.; Zepnik, H.; Wanek, P.; Eder, E.; Dingley, K.; Ihmels, H.; Völkel, W.; Dekant, W. Ochratoxin A: Lack of Formation of Covalent DNA Adducts. *Chemical research in toxicology* **2004**, *17*, 234–242. https://doi.org/10.1021/tx034188m.

(4) Kou, S.-B.; Lou, Y.-Y.; Zhou, K.-L.; Wang, B.-L.; Lin, Z.-Y.; Shi, J.-H. In Vitro Exploration of Interaction Behavior between Calf Thymus DNA and Fenhexamid with the Help of Multi-Spectroscopic Methods and Molecular Dynamics Simulations. *Journal of Molecular Liquids* **2019**, *296*, 112067. https://doi.org/10.1016/j.molliq.2019.112067.

(5) Shi, J.-H.; Zhou, K.-L.; Lou, Y.-Y.; Pan, D.-Q. Multi-Spectroscopic and Molecular Docking Studies on the Interaction of Darunavir, a HIV Protease Inhibitor with Calf Thymus DNA. *Spectrochimica Acta Part A: Molecular and Biomolecular Spectroscopy* **2018**, *193*, 14–22. https://doi.org/10.1016/j.saa.2017.11.061.

(6) Białobrzeska, W.; Niedziałkowski, P.; Malinowska, N.; Cebula, Z.; Ossowski, T. Analysis of Interactions between Calf Thymus DNA and 1,5-Di(Piperazin-1-Yl)Anthracene-9,10-Dione Using Spectroscopic and Electrochemical Methods. *Journal of Molecular Liquids* **2019**, *289*, 111080. https://doi.org/10.1016/j.molliq.2019.111080.

(7) da Silva, C. M.; Silva, M. M.; Reis, F. S.; Ruiz, A. L. T. G.; de Carvalho, J. E.; Santos, J. C. C.; Figueiredo, I. M.; Alves, R. B.; Modolo, L. V.; de Fátima, Â. Studies on Free Radical Scavenging, Cancer Cell Antiproliferation, and Calf Thymus DNA Interaction of Schiff Bases. *Journal of Photochemistry and Photobiology B: Biology* **2017**, *172*, 129–138. https://doi.org/10.1016/j.jphotobiol.2017.05.020.

(8) Rovina, K.; Shaeera, S. N.; Vonnie, J. M.; Yi, S. X. Recent Biosensors Technologies for Detection of Mycotoxin in Food Products. *Mycotoxins and Food Safety* **2019**. https://doi.org/10.5772/intechopen.89022.

(9) Tian, Y.; Larsson, K. Process of Diamond Surface Termination by Carboxylic and Amino Groups: A Quantum Mechanics Approach. *Journal of Material Science & Engineering* **2019**, *08* (01), 1–10. https://doi.org/10.4172/2169-0022.1000506.
(10) Chauhan, S.; Jain, N.; Nagaich, U. Nanodiamonds with Powerful Ability for Drug Delivery and Biomedical Applications: Recent Updates on in Vivo Study and Patents. *Journal of Pharmaceutical Analysis* **2020**, *10* (1), 1–12. https://doi.org/10.1016/j.jpha.2019.09.003.
(11) Kaur, R.; Badea, I. Nanodiamonds as Novel Nanomaterials for Biomedical Applications: Drug Delivery and Imaging Systems. *Int J Nanomedicine* **2013**, *8*, 203–220. https://doi.org/10.2147/IJN.S37348.
(12) Acosta, V.; Hemmer, P. Nitrogen-Vacancy Centers: Physics and Applications. *MRS Bulletin* **2013**, *38* (2), 127–130. https://doi.org/10.1557/mrs.2013.18.
(13) Sękowska, A.; Majchrowicz, D.; Sabisz, A.; Ficek, M.; Bułło-Piontecka, B.; Kosowska, M.; Jing, L.; Bogdanowicz, R.; Szczerska, M. Nanodiamond Phantoms Mimicking Human Liver: Perspective to Calibration of T1 Relaxation Time in Magnetic Resonance Imaging. *Scientific Reports* **2020**, *10* (1), 6446. https://doi.org/10.1038/s41598-020-63581-9.
(14) Wojciechowski, A. M.; Nakonieczna, P.; Mrózek, M.; Sycz, K.; Kruk, A.; Ficek, M.; Głowacki, M.; Bogdanowicz, R.; Gawlik, W. Optical Magnetometry Based on Nanodiamonds with Nitrogen-Vacancy Color Centers. *Materials* **2019**, *12* (18), 2951. https://doi.org/10.3390/ma12182951.
(15) Jelezko, F.; Wrachtrup, J. Single Defect Centres in Diamond: A Review. *physica status solidi (a)* **2006**, *203* (13), 3207–3225. https://doi.org/10.1002/pssa.200671403.
(16) Bourgeois, E.; Gulka, M.; Nesladek, M. Photoelectric Detection and Quantum Readout of Nitrogen-Vacancy Center Spin States in Diamond. *Advanced Optical Materials* **2020**, *8* (12), 1902132. https://doi.org/10.1002/adom.201902132.
(17) Fu, C.-C.; Lee, H.-Y.; Chen, K.; Lim, T.-S.; Wu, H.-Y.; Lin, P.-K.; Wei, P.-K.; Tsao, P.-H.; Chang, H.-C.; Fann, W. Characterization and Application of Single Fluorescent Nanodiamonds as Cellular Biomarkers. *PNAS* **2007**, *104* (3), 727–732. https://doi.org/10.1073/pnas.0605409104.
(18) Barone, F. C.; Marcinkiewicz, C.; Li, J.; Feng, Y.; Sternberg, M.; Lelkes, P. I.; Rosenbaum-Halevi, D.; Gerstenhaber, J. A.; Feuerstein, G. Z. Long-Term Biocompatibility of Fluorescent Diamonds-(NV)-Z~800 Nm in Rats: Survival, Morbidity, Histopathology, Particle Distribution and Excretion Studies (Part IV). *Int J Nanomedicine* **2019**, *14*, 1163–1175. https://doi.org/10.2147/IJN.S189048.
(19) McDonald, M.; Monaco, A.; Vahidpour, F.; Haenen, K.; Giugliano, M.; Nesladek, M. Diamond Microelectrode Arrays for in Vitro Neuronal Recordings. *MRS Communications* **2017**, *7* (3), 683–690. https://doi.org/10.1557/mrc.2017.62.
(20) Wąsowicz, M.; Ficek, M.; Wróbel, M. S.; Chakraborty, R.; Fixler, D.; Wierzba, P.; Jędrzejewska-Szczerska, M. Haemocompatibility of Modified Nanodiamonds. *Materials* **2017**, *10* (4), 352. https://doi.org/10.3390/ma10040352.
(21) Schirhagl, R.; Chang, K.; Loretz, M.; Degen, C. L. Nitrogen-Vacancy Centers in Diamond: Nanoscale Sensors for Physics and Biology. *Annual Review of Physical Chemistry* **2014**, *65* (1), 83–105. https://doi.org/10.1146/annurev-physchem-040513-103659.
(22) Kawai, S.; Yamano, H.; Sonoda, T.; Kato, K.; Buendia, J. J.; Kageura, T.; Fukuda, R.; Okada, T.; Tanii, T.; Higuchi, T.; Haruyama, M.; Yamada, K.; Onoda, S.; Ohshima, T.; Kada, W.; Hanaizumi, O.; Stacey, A.; Teraji, T.; Kono, S.; Isoya, J.; Kawarada, H. Nitrogen-Terminated Diamond Surface for Nanoscale NMR by Shallow Nitrogen-Vacancy Centers. *J. Phys. Chem. C* **2019**, *123* (6), 3594–3604. https://doi.org/10.1021/acs.jpcc.8b11274.
(23) Gibson, N. M.; Luo, T. J. M.; Brenner, D. W.; Shenderova, O. Immobilization of Mycotoxins on Modified Nanodiamond Substrates. *Biointerphases* **2011**, *6* (4), 210–217. https://doi.org/10.1116/1.3672489.
(24) Puzyr', A. P.; Burov, A. E.; Bondar', V. S.; Trusov, Yu. N. Neutralization of Aflatoxin B1 by Ozone Treatment and Adsorption by Nanodiamonds. *Nanotechnol Russia* **2010**, *5* (1), 137–141. https://doi.org/10.1134/S1995078010010143.
(25) Atomistix Toolkit Version 2019.03, Synopsys QuantumWise A/S (Www.Quantumwise.Com).

(26) Kim, S.; Chen, J.; Cheng, T.; Gindulyte, A.; He, J.; He, S.; Li, Q.; Shoemaker, B. A.; Thiessen, P. A.; Yu, B.; Zaslavsky, L.; Zhang, J.; Bolton, E. E. PubChem 2019 Update: Improved Access to Chemical Data. *Nucleic Acids Research* **2019**, *47* (D1), D1102–D1109. https://doi.org/10.1093/nar/gky1033.

(27) Smidstrup, S.; Markussen, T.; Vancraeyveld, P.; Wellendorff, J.; Schneider, J.; Gunst, T.; Verstichel, B.; Stradi, D.; Khomyakov, P. A.; Vej-Hansen, U. G.; Lee, M. E.; Chill, S. T.; Rasmussen, F.; Penazzi, G.; Corsetti, F.; Ojanperä, A.; Jensen, K.; Palsgaard, M. L. N.; Martinez, U.; Blom, A.; Brandbyge, M.; Stokbro, K. QuantumATK: An Integrated Platform of Electronic and Atomic-Scale Modelling Tools. *Journal of Physics Condensed Matter* **2020**, *32* (1). https://doi.org/10.1088/1361-648X/ab4007.

(28) Vashisth, A.; Ashraf, C.; Zhang, W.; Bakis, C. E.; Van Duin, A. C. T. Accelerated ReaxFF Simulations for Describing the Reactive Cross-Linking of Polymers. *Journal of Physical Chemistry A* **2018**, *122* (32), 6633–6642. https://doi.org/10.1021/acs.jpca.8b03826.

(29) Jos; Soler, M.; Emilio, A.; Julian, D. G.; Alberto, G.; Javier, J.; Pablo, O.; Daniel, S.; Nchez, P. The SIESTA Method for Ab Initio Order-N Materials Simulation. *Journal of Physics: Condensed Matter* **2002**, No. 11, 2745. https://doi.org/10.1088/0953-8984/14/11/302.

(30) van Setten, M. J.; Giantomassi, M.; Bousquet, E.; Verstraete, M. J.; Hamann, D. R.; Gonze, X.; Rignanese, G. M. The PSEUDODOJO: Training and Grading a 85 Element Optimized Norm-Conserving Pseudopotential Table. *Computer Physics Communications* **2018**, *226*, 39–54. https://doi.org/10.1016/j.cpc.2018.01.012.

(31) Smidstrup, S.; Stradi, D.; Wellendorff, J.; Khomyakov, P. A.; Vej-Hansen, U. G.; Lee, M.-E.; Ghosh, T.; Jónsson, E.; Jónsson, H.; Stokbro, K. First-Principles Green's-Function Method for Surface Calculations: A Pseudopotential Localized Basis Set Approach. *Physical Review B* **2017**, *96* (19), 195309. https://doi.org/10.1103/PhysRevB.96.195309.

(32) Knizhnik, A. A.; Polynskaya, Y. G.; Sinitsa, A. S.; Kuznetsov, N. M.; Belousov, S. I.; Chvalun, S. N.; Potapkin, B. V. Analysis of Structural Organization and Interaction Mechanisms of Detonation Nanodiamond Particles in Hydrosols. *Phys. Chem. Chem. Phys.* **2021**, *23* (1), 674–682. https://doi.org/10.1039/D0CP05533F.

(33) Yeganeh, M.; Badieian Baghsiyahi, F. Exploring the Sensitivity of Nanodiamond to Sarafloxacin: A DFT Approach. *Journal of Physics and Chemistry of Solids* **2019**, *124*, 235–241. https://doi.org/10.1016/j.jpcs.2018.09.032.

(34) Chou, J.-P.; Gali, A. Nitrogen-Vacancy Diamond Sensor: Novel Diamond Surfaces from Ab Initio Simulations. *MRS Communications* **2017**, *7* (3), 551–562. https://doi.org/10.1557/mrc.2017.75.

(35) Gali, A.; Fyta, M.; Kaxiras, E. Ab Initio Supercell Calculations on Nitrogen-Vacancy Center in Diamond: Electronic Structure and Hyperfine Tensors. *Physical Review B - Condensed Matter and Materials Physics* **2008**, *77* (15), 1–12. https://doi.org/10.1103/PhysRevB.77.155206.

(36) Kaviani, M.; Deák, P.; Aradi, B.; Frauenheim, T.; Chou, J. P.; Gali, A. Proper Surface Termination for Luminescent Near-Surface NV Centers in Diamond. *Nano Letters* **2014**, *14* (8), 4772–4777. https://doi.org/10.1021/nl501927y.

(37) Gali, Á. Ab Initio Theory of the Nitrogen-Vacancy Center in Diamond. *Nanophotonics* **2019**, *8* (11), 1907–1943. https://doi.org/10.1515/nanoph-2019-0154.

(38) Brown, N.; Hod, O. Controlling the Electronic Properties of Nanodiamonds via Surface Chemical Functionalization: A DFT Study. *J. Phys. Chem. C* **2014**, *118* (10), 5530–5537. https://doi.org/10.1021/jp409236t.

(39) Makino, T.; Kato, H.; Shimizu, M.; Hatano, M.; Mizuochi, N. Charge State Control by Band Engineering. In *Semiconductors and Semimetals*; Elsevier, 2020; Vol. 103, pp 137–159. https://doi.org/10.1016/bs.semsem.2020.03.005.

(40) Cui, J. B.; Ristein, J.; Ley, L. Electron Affinity of the Bare and Hydrogen Covered Single Crystal Diamond (111) Surface. *Phys. Rev. Lett.* **1998**, *81* (2), 429–432. https://doi.org/10.1103/PhysRevLett.81.429.

(41) Mackie, W. A.; Plumlee, J. E.; Bell, A. E. Work Function Measurements of Diamond Film Surfaces. *J. Vac. Sci. Technol. B* **1996**, *14* (3), 6.

(42) Maier, F.; Ristein, J.; Ley, L. Electron Affinity of Plasma-Hydrogenated and Chemically Oxidized Diamond (100) Surfaces. *Phys. Rev. B* **2001**, *64* (16), 165411. https://doi.org/10.1103/PhysRevB.64.165411.
(43) Laube, C.; Oeckinghaus, T.; Lehnert, J.; Griebel, J.; Knolle, W.; Denisenko, A.; Kahnt, A.; Meijer, J.; Wrachtrup, J.; Abel, B. Controlling the Fluorescence Properties of Nitrogen Vacancy Centers in Nanodiamonds. *Nanoscale* **2019**, *11* (4), 1770–1783. https://doi.org/10.1039/C8NR07828A.
(44) Skyrianou, K. C.; Psycharis, V.; Raptopoulou, C. P.; Kessissoglou, D. P.; Psomas, G. Nickel-Quinolones Interaction. Part 4. Structure and Biological Evaluation of Nickel(II)-Enrofloxacin Complexes Compared to Zinc(II) Analogues. *J. Inorg. Biochem.* **2011**, *105* (1), 63–74. https://doi.org/10.1016/j.jinorgbio.2010.09.007.
(45) Bera, R.; Sahoo, B. K.; Ghosh, K. S.; Dasgupta, S. Studies on the Interaction of Isoxazolcurcumin with Calf Thymus DNA. *International Journal of Biological Macromolecules* **2008**, *42* (1), 14–21. https://doi.org/10.1016/j.ijbiomac.2007.08.010.
(46) Pakravan, P.; Masoudian, S. Study on the Interaction between Isatin-β-Thiosemicarbazone and Calf Thymus DNA by Spectroscopic Techniques. *Iran J Pharm Res* **2015**, *14* (1), 111–123.
(47) Zhang, X.; Poniewierski, A.; Jelińska, A.; Zagożdżon, A.; Wisniewska, A.; Hou, S.; Hołyst, R. Determination of Equilibrium and Rate Constants for Complex Formation by Fluorescence Correlation Spectroscopy Supplemented by Dynamic Light Scattering and Taylor Dispersion Analysis. *Soft Matter* **2016**, *12* (39), 8186–8194. https://doi.org/10.1039/C6SM01791F.
(48) Mehran, S.; Rasmi, Y.; Karamdel, H. R.; Hossinzadeh, R.; Gholinejad, Z. Study of the Binding Interaction between Wortmannin and Calf Thymus DNA: Multispectroscopic and Molecular Docking Studies https://www.hindawi.com/journals/ecam/2019/4936351/ (accessed 2020 -09 -02). https://doi.org/10.1155/2019/4936351.
(49) Zhang, G.; Fu, P.; Wang, L.; Hu, M. Molecular Spectroscopic Studies of Farrerol Interaction with Calf Thymus DNA. *J. Agric. Food Chem.* **2011**, *59* (16), 8944–8952. https://doi.org/10.1021/jf2019006.
(50) Ma, L.; Wang, J.; Zhang, Y. Probing the Characterization of the Interaction of Aflatoxins B1 and G1 with Calf Thymus DNA In Vitro. *Toxins (Basel)* **2017**, *9* (7). https://doi.org/10.3390/toxins9070209.
(51) Fluorescence Sensing. In *Principles of Fluorescence Spectroscopy*; Lakowicz, J. R., Ed.; Springer US: Boston, MA, 2006; pp 623–673. https://doi.org/10.1007/978-0-387-46312-4_19.
(52) Su, Z.; Ren, Z.; Bao, Y.; Lao, X.; Zhang, J.; Zhang, J.; Zhu, D.; Lu, Y.; Hao, Y.; Xu, S. Luminescence Landscapes of Nitrogen-Vacancy Centers in Diamond: Quasi-Localized Vibrational Resonances and Selective Coupling. *J. Mater. Chem. C* **2019**, *7* (26), 8086–8091. https://doi.org/10.1039/C9TC01954E.
(53) Chen, L.; Miao, X.; Ma, H.; Guo, L.; Wang, Z.; Yang, Z.; Fang, C.; Jia, X. Synthesis and Characterization of Diamonds with Different Nitrogen Concentrations under High Pressure and High Temperature Conditions. *CrystEngComm* **2018**, *20* (44), 7164–7169. https://doi.org/10.1039/C8CE01533C.
(54) Yang, M.; Yuan, Q.; Gao, J.; Shu, S.; Chen, F.; Sun, H.; Nishimura, K.; Wang, S.; Yi, J.; Lin, C.-T.; Jiang, N. A Diamond Temperature Sensor Based on the Energy Level Shift of Nitrogen-Vacancy Color Centers. *Nanomaterials* **2019**, *9* (11), 1576. https://doi.org/10.3390/nano9111576.
(55) Bourgeois, E.; Gulka, M.; Nesladek, M. Photoelectric Detection and Quantum Readout of Nitrogen-Vacancy Center Spin States in Diamond. *Advanced Optical Materials* **2020**, *8* (12), 1902132. https://doi.org/10.1002/adom.201902132.
(56) Lin, H.; Li, Z.; Lu, H.; Sun, S.; Chen, F.; Wei, K.; Ming, D. Robust Classification of Tea Based on Multi-Channel LED-Induced Fluorescence and a Convolutional Neural Network. *Sensors* **2019**, *19* (21), 4687. https://doi.org/10.3390/s19214687.
(57) Li, Y.; Zhang, G.; Tao, M. Binding Properties of Herbicide Chlorpropham to DNA: Spectroscopic, Chemometrics and Modeling Investigations. *Journal of Photochemistry and Photobiology B: Biology* **2014**, *138*, 109–117. https://doi.org/10.1016/j.jphotobiol.2014.05.011.

(58) Labieniec, M.; Gabryelak, T. Interactions of Tannic Acid and Its Derivatives (Ellagic and Gallic Acid) with Calf Thymus DNA and Bovine Serum Albumin Using Spectroscopic Method. *J Photochem Photobiol B* **2006**, *82* (1), 72–78. https://doi.org/10.1016/j.jphotobiol.2005.09.005.
(59) Nafisi, S.; Manouchehri, F.; Tajmir-Riahi, H.-A.; Varavipour, M. Structural Features of DNA Interaction with Caffeine and Theophylline. *Journal of Molecular Structure* **2008**, *875* (1), 392–399. https://doi.org/10.1016/j.molstruc.2007.05.010.
(60) Chakrapani, V.; Angus, J. C.; Anderson, A. B.; Wolter, S. D.; Stoner, B. R.; Sumanasekera, G. U. Charge Transfer Equilibria Between Diamond and an Aqueous Oxygen Electrochemical Redox Couple. *Science* **2007**, *318* (5855), 1424–1430. https://doi.org/10.1126/science.1148841.
(61) Il'ichev, Y. V.; Perry, J. L.; Simon, J. D. Interaction of Ochratoxin A with Human Serum Albumin. Preferential Binding of the Dianion and PH Effects. *J. Phys. Chem. B* **2002**, *106* (2), 452–459. https://doi.org/10.1021/jp012314u.
(62) Gao, T.; Zhang, W.; Wang, Y.; Yang, G. DNA Compaction and Charge Neutralization Regulated by Divalent Ions in Very Low PH Solution. *Polymers* **2019**, *11* (2), 337. https://doi.org/10.3390/polym11020337.
(63) Saha, M.; Nandy, P.; Chakraborty, M.; Das, P.; Das, S. The Importance of PKa in an Analysis of the Interaction of Compounds with DNA. *Biophysical Chemistry* **2018**, *236*, 15–21. https://doi.org/10.1016/j.bpc.2018.02.001.
(64) Miller, B. S.; Bezinge, L.; Gliddon, H. D.; Huang, D.; Dold, G.; Gray, E. R.; Heaney, J.; Dobson, P. J.; Nastouli, E.; Morton, J. J. L.; McKendry, R. A. Spin-Enhanced Nanodiamond Biosensing for Ultrasensitive Diagnostics. *Nature* **2020**, *587* (7835), 588–593. https://doi.org/10.1038/s41586-020-2917-1.
(65) Zhao, L.; Nakae, Y.; Qin, H.; Ito, T.; Kimura, T.; Kojima, H.; Chan, L.; Komatsu, N. Polyglycerol-Functionalized Nanodiamond as a Platform for Gene Delivery: Derivatization, Characterization, and Hybridization with DNA. *Beilstein J Org Chem* **2014**, *10*, 707–713. https://doi.org/10.3762/bjoc.10.64.
(66) Petrakova, V.; Benson, V.; Buncek, M.; Fiserova, A.; Ledvina, M.; Stursa, J.; Cigler, P.; Nesladek, M. Imaging of Transfection and Intracellular Release of Intact, Non-Labeled DNA Using Fluorescent Nanodiamonds. *Nanoscale* **2016**, *8* (23), 12002–12012. https://doi.org/10.1039/C6NR00610H.